

Article

# Dynamic Study of a Rooftop Vertical Axis Wind Turbine Tower Based on an Automated Vibration Data Processing Algorithm

Ying Wang <sup>1</sup>, Wensheng Lu <sup>1</sup>, Kaoshan Dai <sup>2,1,\*</sup> , Miaomiao Yuan <sup>1</sup> and Shen-En Chen <sup>3</sup> 

<sup>1</sup> State Key Laboratory of Disaster Reduction in Civil Engineering, Tongji University, Shanghai 200092, China; tj\_wangying@foxmail.com (Y.W.); wally@tongji.edu.cn (W.L.); 209jgsys@tongji.edu.cn (M.Y.)

<sup>2</sup> Department of Civil Engineering, Sichuan University, Chengdu 610065, China

<sup>3</sup> Department of Civil & Environmental Engineering, University of North Carolina, Charlotte, NC 28223, USA; schen12@uncc.edu

\* Correspondence: kdai@scu.edu.cn; Tel.: +86-28-8599-6688

Received: 3 July 2018; Accepted: 6 August 2018; Published: 13 November 2018



**Abstract:** When constructed on tall building rooftops, the vertical axis wind turbine (VAWT) has the potential of power generation in highly urbanized areas. In this paper, the ambient dynamic responses of a rooftop VAWT were investigated. The dynamic analysis was based on ambient measurements of the structural vibration of the VAWT (including the supporting structure), which resides on the top of a 24-story building. To help process the ambient vibration data, an automated algorithm based on stochastic subspace identification (SSI) with a fast clustering procedure was developed. The algorithm was applied to the vibration data for mode identification, and the results indicate interesting modal responses that may be affected by the building vibration, which have significant implications for the condition monitoring strategy for the VAWT. The environmental effects on the ambient vibration data were also investigated. It was found that the blade rotation speed contributes the most to the vibration responses.

**Keywords:** vertical axis wind turbine; structural health monitoring; operational modal analysis; stochastic subspace identification; vibration test

## 1. Introduction

In commercial wind-power generation, most attention is placed on the deployment of horizontal axis wind turbines (HAWTs) as they are thought to be more efficient than the vertical axis wind turbines (VAWTs) [1]. However, recent studies on VAWTs found that they can be driven by gentler winds and have no need of yaw. These advantages make VAWTs ideal for urban power generation [1,2].

VAWTs can be generally divided into two types: drag-type and lift-type. Lift-type VAWTs have a bigger tip-speed ratio; thus, they can convert the highest amount of energy. Lift-type VAWTs, such as the Darrieus rotor with egg-beater blades ( $\Phi$ -type) and the Darrieus rotor with straight blades (H-type), are the most widely used VAWTs [3,4]. Furthermore, their designs were improved with computer fluid dynamics (CFD) and finite element analysis (FEA), making them more efficient in energy conversion [5–7]. However, studies on VAWTs are limited when compared to those on horizontal wind turbines. Although several laboratory vibration tests were performed to study the dynamic behavior of VAWTs [8–11], only a limited number of field vibration measurements were conducted. Some studies showed that the vibration of the VAWT support structure may be influenced by the wind turbine's operation [9]. Although there are some research reports about the development of rooftop VAWTs which can make better use of high-altitude winds [12,13], very few instances of on-site monitoring are published.

The implementation of structural health monitoring (SHM) systems in a structure can help ensure optimal performances of the structure. This is achieved via real-time vibration measurements and a better understanding of the dynamic loads [14–16]. The SHM of wind turbine towers was proposed for system monitoring and was integrated into the Supervisory Control and Data Acquisition (SCADA) systems [17–20]. The SHM of HAWT towers concerns problems including resonance responses caused by operation frequency or blade passing frequency [21–23], foundation scouring [24], blade flange conditions [25], and structural performances under extreme events [26,27].

Understanding the dynamics of VAWTs can be helpful for improving the design of VAWTs and the implementation of SHM in the VAWT systems. In this paper, along with the installation of an H-type VAWT on the roof of a 24-story dormitory building, a structural health monitoring system was implemented, and the dynamic responses of the VAWT were studied and reported. The objective of this study was to understand how the VAWT behaves dynamically under normal operation conditions. Ambient vibration measurements were obtained for both the building and the VAWT, including the support tower. The data were analyzed to find the interactions between the building and the VAWT structure, as well as the environmental effects on the vibration responses. To facilitate modal parameter identification, an automated algorithm based on stochastic subspace identification (SSI) and a fast clustering algorithm was developed. The results are presented herein along with discussions on the interactions between the building and the tower and their significance for condition monitoring.

The paper is organized as follows: in Section 2, the VAWT is firstly introduced and the vibration measurement campaign is described. Data analyses and a discussion of the results are provided in Sections 3 and 4, respectively. The findings are summarized in Section 5.

## 2. The VAWT Wind Turbine and Vibration Measurements

An H-type VAWT was installed on the roof of a 24-story dormitory building belonging to the Tongji University, Shanghai, China (referred to as the #6 building at the Zhangwu campus).

Vibration measurements of the #6 building were conducted prior to the VAWT installation. Several electromagnetic accelerometers were placed on the building's rooftop, and the lateral movements of the building along both the X-direction (longer axis) and the Y-direction (shorter axis) were measured. These electromagnetic accelerometers, with a moving coil as the sensing unit, have good performances in the low-frequency range. Details of the electromagnetic accelerometers can be found in Table 1. Figure 1 shows the #6 building, the relative location of the VAWT, and the deployment of the vibration sensors. Accelerations of the roof of the #6 building were measured with a sampling frequency of 128 Hz, and the duration of the building acceleration data was around 9 min.

**Table 1.** Details of accelerometers used for building and tower testing.

Item	Piezoelectric Sensors (Tower)	Electromagnetic Sensors (Building)
Sensitivity	9.83 mV/(ms <sup>2</sup> )	329 mV/(ms <sup>2</sup> )
Resolution	0.001 ms <sup>2</sup>	3 × 10 <sup>-6</sup> ms <sup>2</sup>
Frequency range	1.0 to 5000 Hz (±5%) 0.5 to 7000 Hz (±10%)	0.25 to 100 Hz (+1 dB to -3 dB)
Acceleration range	500 ms <sup>2</sup>	200 ms <sup>2</sup>
Weight	4.4 g	800 g

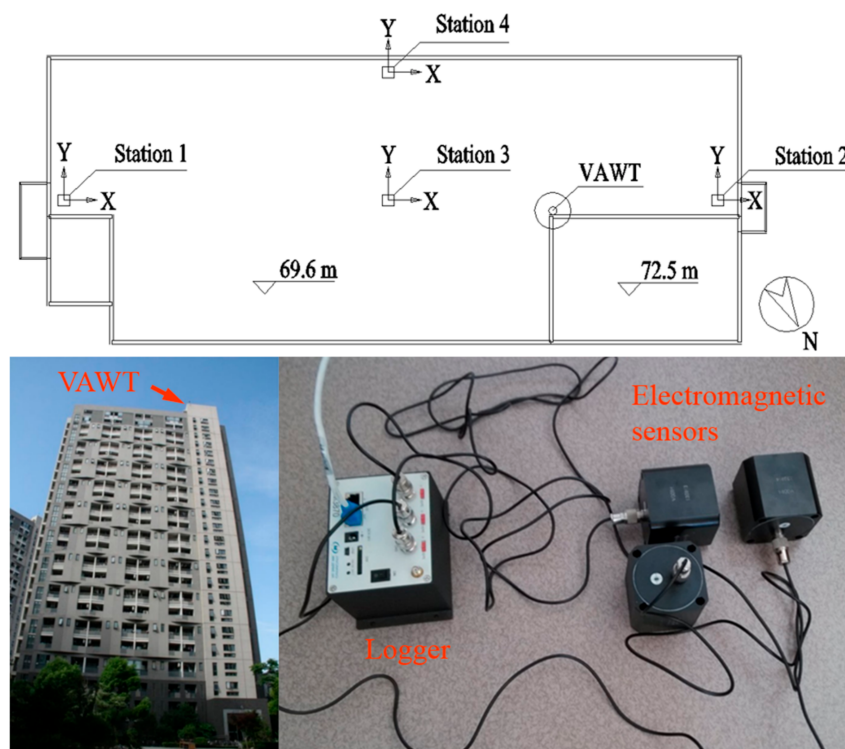
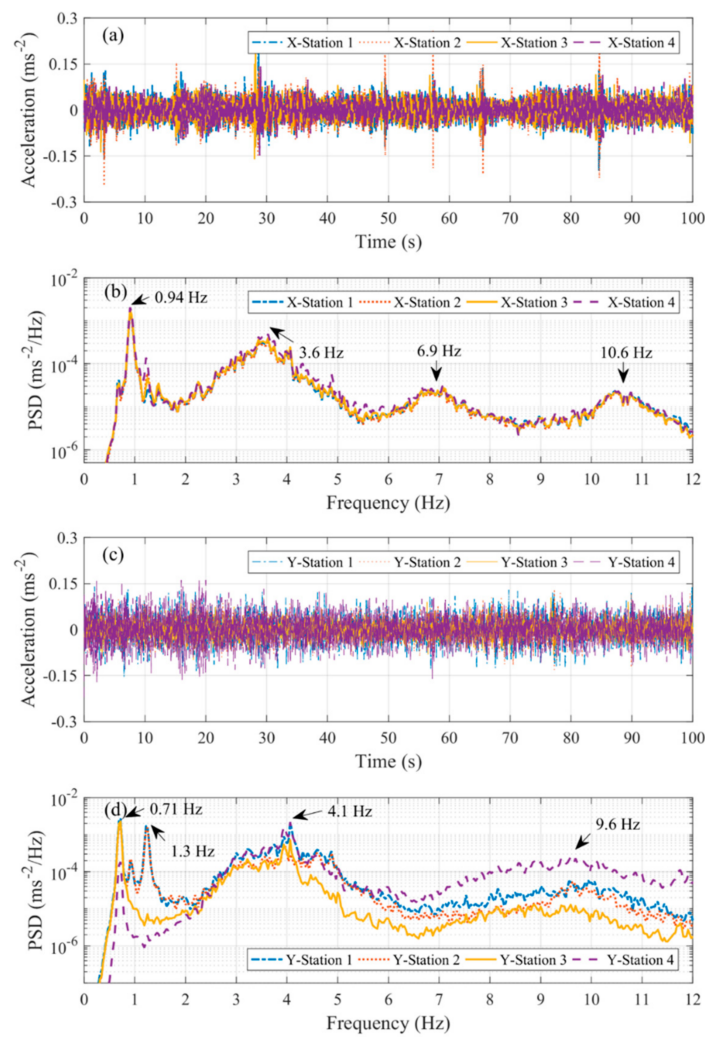


Figure 1. Sensor deployment on the #6 building's roof.

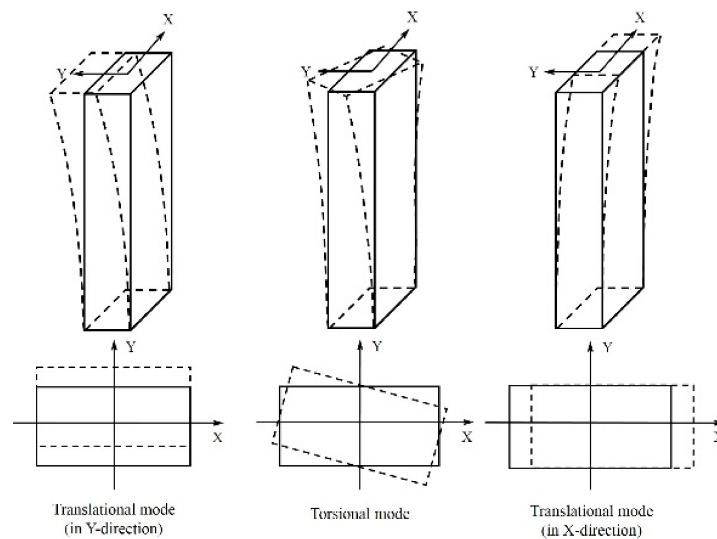
Both the vibration-time histories and the power spectrum density (PSD) of the roof were obtained along the X- and Y-directions. The building vibrations obtained are shown in Figure 2. Based on the PSD diagram, the first few modes of natural frequencies of the #6 building are shown to be less than 12 Hz (Table 2). The peaks of higher vibration modes are not as obvious as the lower modes; thus, high-frequency modes are more difficult to determine (Figure 2b,d). The frequencies shown in Table 2 were the measured natural frequencies of the #6 building. The roof vibrations, shown in Figure 3, include (1) translational motion along the X-direction, (2) translational motion along the Y-direction, and (3) torsional motion. Since the long axis of the building is along the X-direction, the torsional motion (corresponding to 1.3 Hz) can be observed for the Y-direction measurements of Station 1 and Station 2, indicating possibly more torsional vibration for a substructure (e.g., a VAWT) if it is installed on the edge of a building than for one installed at the center of the building.

Table 2. Natural frequencies of the #6 building.

Direction	Frequency (Hz)			
	1st	2nd	3rd	4th
X	0.94	3.60	6.90	10.60
Y	0.71	1.30	4.10	9.60



**Figure 2.** Ambient responses of the #6 building’s roof: (a) time histories along the X-direction; (b) power spectrum density (PSD) along the X-direction; (c) time histories along the Y-direction; (d) PSD along the Y-direction.



**Figure 3.** Building mode shape sketch.

The VAWT consists of a power generation component that includes five turbine blades, a deflector, a generator, and a hollow shaft. Figure 4 shows the wind turbine, which is attached via metal-strip hoops to the exterior of an extension structure for the elevator shaft on the rooftop. The design details of the VAWT are listed in Table 3. The metal-strip hoops were designed to laterally constrain the wind turbine tower and were embedded into the wall of the #6 building with expansion bolts. To reduce vibration of the tower, rubber gaskets were placed between the hoops and the tower. There were three hoops attached to the structure with the last hoop very close to the base block. Details of the hoops can be seen in Figure 4. The heavy concrete base block, laid on the roof, was used to weigh down the tower. Bolts were embedded into the concrete base block (foundation) and were connected to the bottom flange of the tower. The bolt size and anchor depth are shown in Table 4.

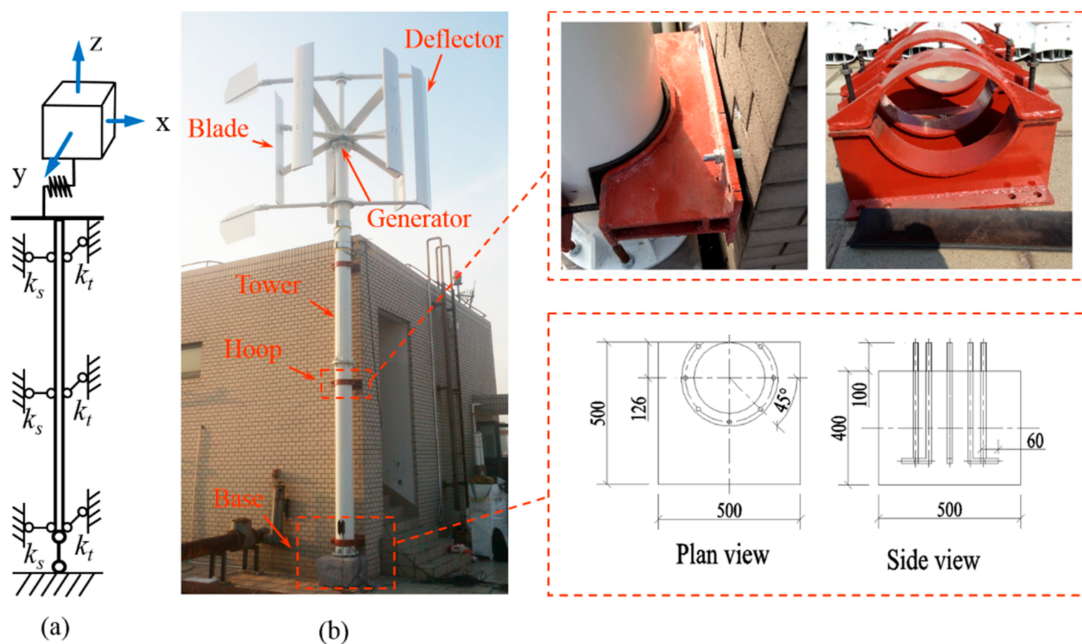


**Figure 4.** The H-type vertical axis wind turbine (VAWT): (a) modeling of the vibration system; (b) the VAWT and the details of its supports (including schematics; unit: mm).

**Table 3.** Details of the wind turbine.

Parameter	Value
Rated power	2 kW
Rated spin speed	250 rpm
Rated wind speed	25 m/s
Maximum design wind speed	32 m/s
Blade height	2 m
Blade span	2.2 m
Weight (generator + blades)	240 kg

**Table 4.** Details of the supports of the wind turbine.

<b>Hoop</b>	
Thickness	6 mm
Material	Q235 steel
Bolts	M10
Expansion bolts	M12
Anchorage depth	≥75 mm
Rubber gasket thickness	5 mm
<b>Tower</b>	
Thickness	4 mm
Material	Q235 steel
External diameter	250 mm
<b>Base</b>	
Bolts	M18

The theoretical frequencies of the VAWT structure were also calculated before the installation to avoid the resonance issue, considering building vibrations. The vibration responses of interest for the wind turbine are the lateral movements of the power generation component as described in the simplified model shown in Figure 4a [28]. Other than the rigid foundation at the base, the bending behaviors of the tower are critically limited by the stiffness of the three hoop supports on the tower shaft. As shown in Figure 4, the hoops consist of half-rings connected to the hoop base using the bolt connectors and rubber gaskets. Hence, the constraining actions of the hoops can be described as shear in the perpendicular direction to the bolts (X-direction) and tension in the bolt connection direction (Y-direction). Also shown in Figure 4 is the simplified dynamic model of the monitoring system, which includes the wind generation component (rigid mass) and the connection to the top hoop support (rod). Different stiffness models can be constructed for the hoop support. The tensile stiffness of a single hoop,  $k_t$ , can be described as

$$k_t = \frac{1}{\frac{1}{2k_{M10}} + \frac{1}{4k_{M12}} + \frac{1}{2k_R}}, \quad (1)$$

where  $k_{M10}$ ,  $k_{M12}$ , and  $k_R$  are the tensile stiffness of M10 bolts and M12 bolts, and the compression stiffness of the rubber gaskets, respectively. The shear stiffness of a single hoop  $k_s$  can be described as

$$k_s = \frac{4k_{M12,s}k_R}{4k_{M12,s} + k_R}, \quad (2)$$

where  $k_{M12,s}$  is the shear stiffness of the M12 bolts. In the following discussion, the vibration responses of the wind turbine are separated into the shear (X) direction and the tension (Y) direction. Using this very simplistic dynamic model, the fundamental frequencies of the tower were derived as 7.2 Hz in the shear direction (X-direction of the tower shaft and X-direction of the building) and 6.0 Hz in the tension direction (Y-direction of the tower shaft and Y-direction of the building).

A monitoring system was designed for the data collection, storage, and processing. Parameters associated with environment, power generation, and structural performances were collected continuously. Measurements were stored in a computer installed on the roof. The system was also designed to allow remote monitoring of data. Figure 5 shows the monitoring setup of the VAWT tower. In this case, a third-generation (3G) network was used for the wireless data transmission. This paper focuses on vibration data collected from this condition monitoring system.

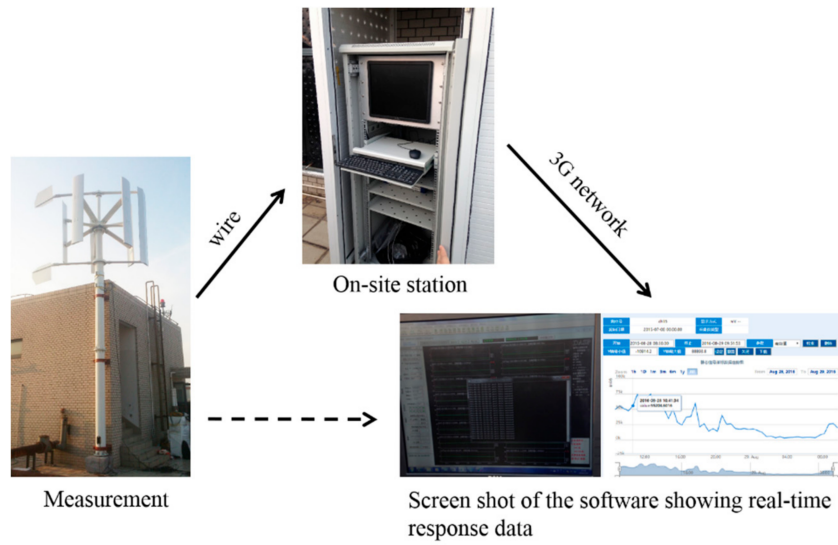


Figure 5. Monitoring setup of the VAWT tower.

To measure the vibration modes of the wind turbine, along with the installation of the VAWT, three pairs of piezoelectric accelerometers were mounted along the tower at three sections with different heights; each pair had two sensors, deployed in two directions perpendicular to each other at each section: (a) the X-direction which runs perpendicular to the hoop bolts (shear direction), and (b) the Y-direction which parallels the tensioning of the hoop bolts. Figure 6 shows the sensor locations, which were designated as cross Sections 1–3. Sensors in cross Section 1 (the generator) were installed inside the tower shaft; thus, the set-up was not influenced by the rotating blades. The other section sensors were installed on the outside surface of the tower. Different from electromagnetic sensors, a piezoelectric sensor adopts a piezoelectric crystal as the sensing unit, and it can be made into a smaller size compared to that of the electromagnetic ones. Details of the piezoelectric accelerometers deployed for tower testing can be found in Table 1.

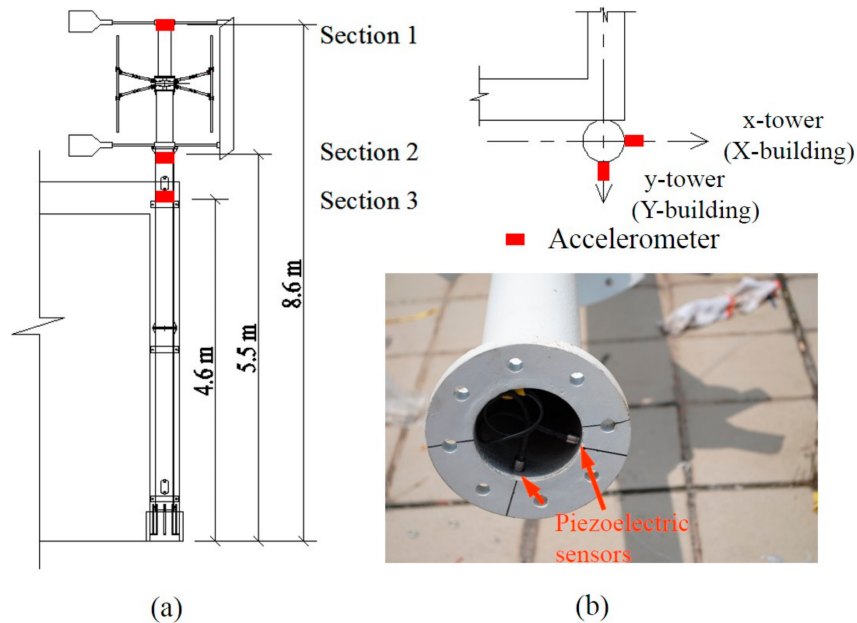
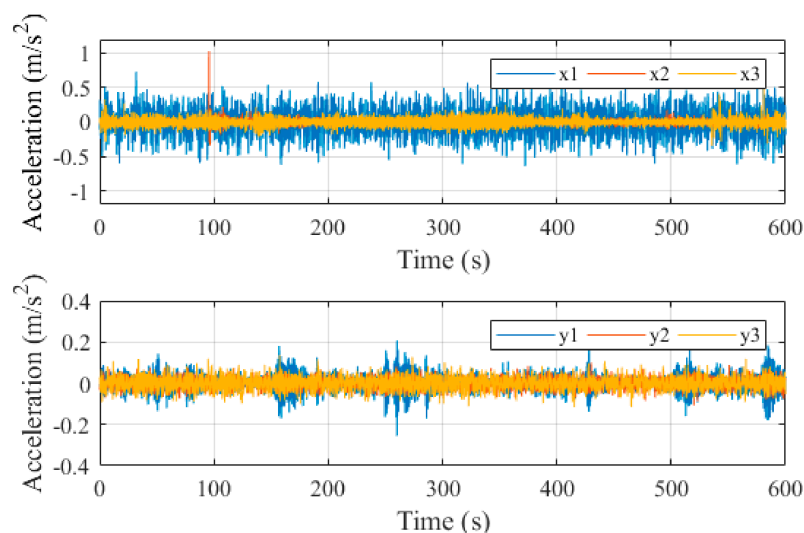


Figure 6. Deployment of sensors: (a) schematics of the VAWT wind turbine; (b) the sensor attachments.

To monitor the environmental conditions, a tachometer, a thermometer, and a voltmeter were also installed. The tachometer was used to measure the rotation speed of the wind turbine. The thermometer kept track of the daily environmental temperature changes near the structure. The power generation of the wind turbine in Watts could be translated from the measurements obtained by the voltmeter. The sampling frequencies of all the measured data were set at 1024 Hz. Typical acceleration time histories for a time window of 10 min are shown in Figure 7. Accelerations labeled x1, x2, and x3, and y1, y2, and y3 correspond to cross Sections 1–3 along the X-direction and the Y-direction of the tower, respectively. Typical time histories in a day (24 h) of rotation speed, temperature, and voltage (power generation) recorded on 28 August 2016 are presented in Figure 8.

A cup anemometer with a wind-direction indicator was installed near the VAWT, which measured the speed and direction of the incoming wind. The anemometer was the F220S model manufactured by the Nanhua Electronics Company, Shanghai, China. Measurements of wind speed and wind direction were recorded about every 10 s. The definition of wind direction was as follows:  $0^\circ$  corresponded to the north direction, and  $90^\circ$  corresponded to the east direction. Since the wind field in urban areas can be quite complex, both the wind speed and direction measurements fluctuated constantly. Only the moving averages with a step length of 10 min were used in current study. Figure 9 shows a typical recorded wind scenario throughout a day (28 August 2016) and its moving average. It can be seen from Figures 8 and 9 that both the maximum wind speed and the maximum temperature occurred at noon, and the temperature and the wind speed were strongly correlated. The rotation speed, which should be linear to the quadratic of the wind speed, only had a medium correlation (the correlation coefficient was 0.581) with the raw wind speed, and was strongly correlated (the correlation coefficient was 0.888) with the average wind speed. This happened since the rotation of the VAWT calls for a continuous wind force rather than a gust. The correlation coefficients between the rotation speed, wind speed, and temperature calculated with both raw wind-speed data and averaged wind-speed data are shown in Table 5. The relationship between the power and the wind speed is also provided in Figure 10.



**Figure 7.** VAWT accelerations at 12 a.m. on 28 August 2016.

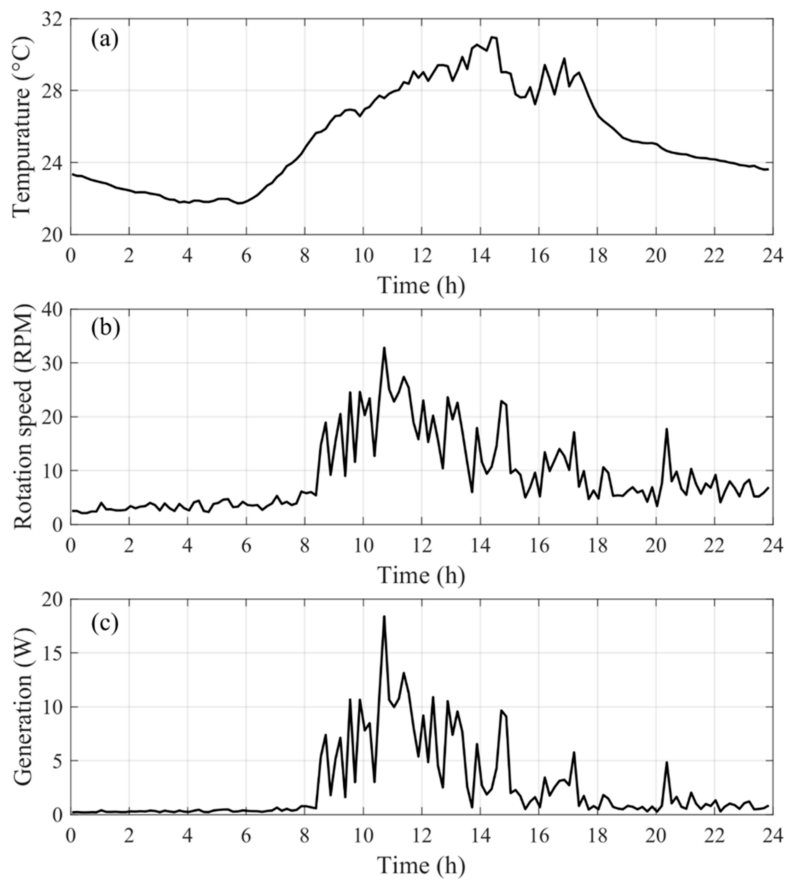


**Figure 8.** Typical monitoring data, recorded on on 28 August 2016: (a) wind turbine rotational speed; (b) temperature; (c) power generation distribution.

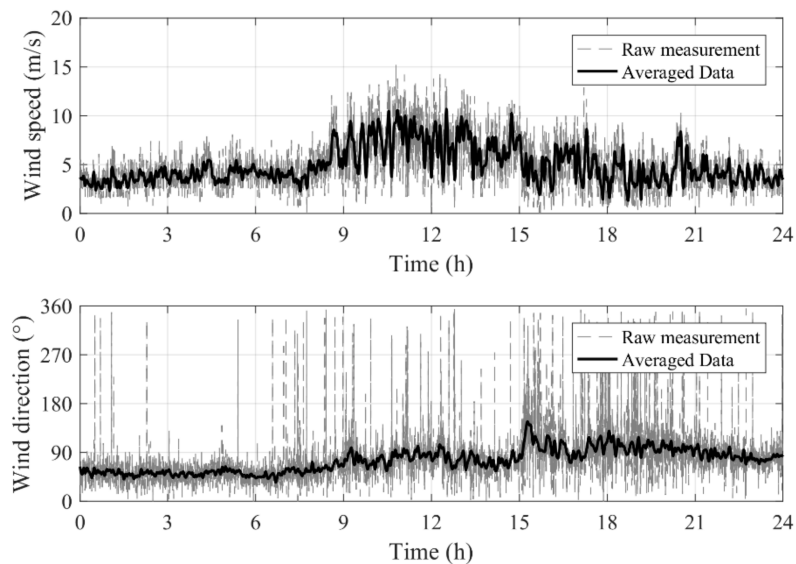


**Figure 9.** Wind speed and wind direction on 28 August 2016.

**Table 5.** Correlation coefficients between rotation speed, wind speed, and temperature.

Correlation Coefficients	Rotation Speed <sup>1/2</sup>	Wind Speed (Raw Data)	Temperature
Rotation speed	1	0.581	0.757
Wind speed	0.581	1	0.516
Temperature	0.757	0.516	1
Correlation Coefficients	Rotation Speed <sup>1/2</sup>	Wind Speed (Moving Average)	Temperature
Rotation speed	1	0.888	0.757
Wind speed	0.888	1	0.677
Temperature	0.757	0.677	1

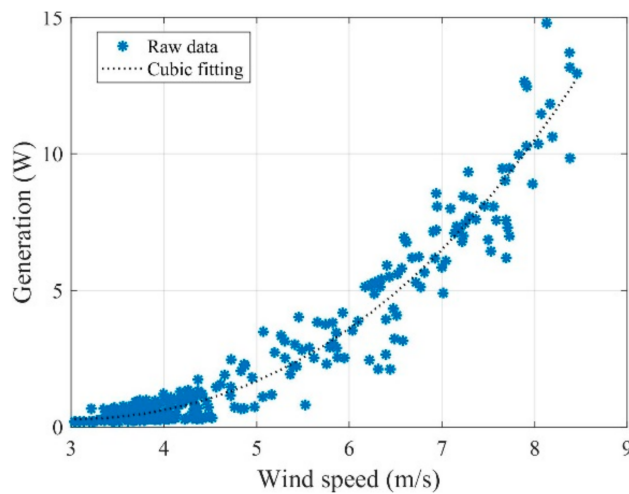


**Figure 10.** Power curve of the rooftop VAWT on 28 August 2016.

### 3. Data Analysis

#### 3.1. Frequency Domain Analyses

The frequency domain analyses were conducted using the power spectrum density (PSD). The PSD of the ambient response of a structure can be written as

$$P_{XX}(f) \propto [T(f)]I[T(f)]^T, \tag{3}$$

where  $P_{XX}(f)$  is the PSD of the response of a structure,  $T(f)$  is the transfer function, which contains the information of a structure, and  $I$  is a unit matrix since the ambient excitation can be regarded as white noise.  $P_{XX}(f)$  represents the system characteristics of a structure, and the period gram method was used to calculate the PSDs. The period gram method uses windows to divide data into sections, and averages the PSDs of each section; hence, it can help accentuate the modal amplitudes and suppress the noise base in the frequency domain [29,30].

#### 3.2. SSI Method

The classical SSI method is based on the state-space model of a system. A discrete-time state-space model of the system under ambient excitation without feedback signals can be described as

$$\begin{cases} \mathbf{x}_{k+1} = \mathbf{A}\mathbf{x}_k + \mathbf{w}_k \\ \mathbf{y}_k = \mathbf{C}\mathbf{x}_k + \mathbf{v}_k \end{cases}, \tag{4}$$

where the subscript  $k$  is the time,  $\mathbf{x}_k$  is the state vector,  $\mathbf{y}_k$  is a measurement vector,  $\mathbf{w}_k$  is an excitation vector that is considered as white noise,  $\mathbf{v}_k$  is a measurement noise vector,  $\mathbf{A}$  is a state transition matrix, and  $\mathbf{C}$  is an output location matrix.

The key to obtaining the modal parameters of the system is to solve for the state transition matrix  $\mathbf{A}$ , and to calculate its eigenvalues and eigenvectors. The procedure of the classical SSI method to obtain the modal parameters of a system is explained below [31,32].

Suppose the number of measurement is  $m$ . A Hankel matrix with  $2i$  row blocks and  $j$  columns can be constructed as

$$\mathbf{H}_{0|2i-1} = \begin{bmatrix} \mathbf{y}_0 & \mathbf{y}_1 & \mathbf{y}_2 & \cdots & \mathbf{y}_{j-1} \\ \mathbf{y}_1 & \mathbf{y}_2 & \mathbf{y}_3 & \cdots & \mathbf{y}_j \\ \cdots & \cdots & \cdots & \cdots & \cdots \\ \mathbf{y}_{i-1} & \mathbf{y}_i & \mathbf{y}_{i+1} & \cdots & \mathbf{y}_{i+j-2} \\ \mathbf{y}_i & \mathbf{y}_{i+1} & \mathbf{y}_{i+2} & \cdots & \mathbf{y}_{i+j-1} \\ \mathbf{y}_{i+1} & \mathbf{y}_{i+2} & \mathbf{y}_{i+3} & \cdots & \mathbf{y}_{i+j} \\ \cdots & \cdots & \cdots & \cdots & \cdots \\ \mathbf{y}_{2i-1} & \mathbf{y}_{2i} & \mathbf{y}_{2i+1} & \cdots & \mathbf{y}_{2i+2j-2} \end{bmatrix}_{2mi \times j} = \begin{bmatrix} \mathbf{H}_{0|i-1} \\ \mathbf{H}_{i|2i-1} \end{bmatrix} = \begin{bmatrix} \mathbf{H}_p \\ \mathbf{H}_f \end{bmatrix}, \quad (5)$$

where  $\mathbf{H}_{0|i-1}$  and  $\mathbf{H}_{i|2i-1}$  are matrices representing the first  $mi$  rows and the second  $mi$  rows of  $\mathbf{H}_{0|2i-1}$ , respectively; and  $\mathbf{H}_p$  and  $\mathbf{H}_f$  are equal to  $\mathbf{H}_{0|i-1}$  and  $\mathbf{H}_{i|2i-1}$ , respectively, with subscripts  $p$  and  $f$  standing for past and future times.

With the orthogonal projection of  $\mathbf{H}_f$  to  $\mathbf{H}_p$ , the projection matrix  $\mathbf{O}_i$  is obtained as

$$\mathbf{O}_i = \mathbf{H}_f / \mathbf{H}_p = \mathbf{H}_f \mathbf{H}_p^T (\mathbf{H}_p \mathbf{H}_p^T)^+ \mathbf{H}_p, \quad (6)$$

where  $(*)^+$  denotes the pseudo-inverse of a matrix.

The projection matrix  $\mathbf{O}_i$  can be decomposed further using the singular-value decomposition, which gives

$$\mathbf{O}_i = \mathbf{U}_i \boldsymbol{\Sigma}_i \mathbf{V}_i^T = \begin{pmatrix} \mathbf{U}_{i1} & \mathbf{U}_{i2} \end{pmatrix} \begin{pmatrix} \boldsymbol{\Sigma}_{i1} & \\ & \boldsymbol{\Sigma}_{i2} = 0 \end{pmatrix} \begin{pmatrix} \mathbf{V}_{i1}^T \\ \mathbf{V}_{i2}^T \end{pmatrix} = \mathbf{U}_{i1} \boldsymbol{\Sigma}_{i1} \mathbf{V}_{i1}^T, \quad (7)$$

where  $\boldsymbol{\Sigma}_i$  is a diagonal matrix of dimension  $mi \times j$ ;  $\mathbf{U}_i$  and  $\mathbf{V}_i$  are orthogonal matrices of dimensions  $mi \times mi$  and  $mi \times j$ , respectively;  $\boldsymbol{\Sigma}_{i1}$  and  $\boldsymbol{\Sigma}_{i2}$  are submatrices of  $\boldsymbol{\Sigma}_i$  that have dimensions  $2n \times 2n$  and  $(mi - 2n) \times (j - 2n)$ , respectively, in which  $n$  is the degree of freedom of the system;  $\mathbf{U}_{i1}$  and  $\mathbf{U}_{i2}$  are submatrices of  $\mathbf{U}_i$ ; and  $\mathbf{V}_{i1}$  and  $\mathbf{V}_{i2}$  are the submatrices of  $\mathbf{V}_i$ . Finally, the observability matrix  $\boldsymbol{\Gamma}_i$  and the Kalman filter state sequence  $\hat{\mathbf{X}}_i$  can be obtained as

$$\boldsymbol{\Gamma}_i = \mathbf{U}_{i1} \boldsymbol{\Sigma}_{i1}^{1/2}, \quad (8)$$

$$\hat{\mathbf{X}}_i = \boldsymbol{\Sigma}_{i1}^{-1/2} \mathbf{V}_{i1}^T. \quad (9)$$

The state transition matrix  $\mathbf{A}$  can then be obtained as

$$\mathbf{A} = \boldsymbol{\Gamma}_1^+ \boldsymbol{\Gamma}_2, \quad (10)$$

where  $\boldsymbol{\Gamma}_1$  and  $\boldsymbol{\Gamma}_2$  are formed as the first  $m \times (i - 1)$  and last  $m \times (i - 1)$  rows of  $\boldsymbol{\Gamma}_i$ , respectively. Eigenvalues and eigenvectors of  $\mathbf{A}$  can be obtained using eigenvalue decomposition:

$$\mathbf{A} = \boldsymbol{\Psi} \boldsymbol{\Lambda} \boldsymbol{\Psi}^{-1}, \quad (11)$$

where  $\Lambda = \text{diag}(\lambda_1 \lambda_2 \dots \lambda_r \dots \lambda_{2n})$ , in which  $\lambda_r$  is the  $r$ -th eigenvalue of  $\mathbf{A}$  and  $\Psi = \begin{pmatrix} \psi_1 & \psi_2 & \dots & \psi_r & \dots & \psi_{2n} \end{pmatrix}$ . The  $r$ -th natural frequency of the system in Hz can be calculated as

$$f_r = \frac{\text{abs}(\ln(\lambda_r) \times f_s)}{2\pi}, \quad (12)$$

where  $f_s$  is the sampling frequency in Hz, and the  $r$ -th damping-ratio of the system can be calculated as

$$\zeta_r = \frac{-\text{real}(\ln(\lambda_r) \times f_s)}{\text{abs}(\ln(\lambda_r) \times f_s)}. \quad (13)$$

The associated mode shape can be calculated as

$$\varphi_r = \mathbf{C}\psi_r, \quad (14)$$

where the measurement matrix  $\mathbf{C}$  is formed as the first  $m$  row of  $\Gamma_i$ .

In this study, the stability diagrams were used to assist the identification of the “stable” modes. In a stability diagram, there are user-defined stability criteria for natural frequencies and for damping ratios. When an identified modal parameter corresponding to the calculation order of  $2n$  is different from that corresponding to the order  $2n - 2$ , which is lower than the threshold of a criterion for the identified parameter, then the criterion is considered to meet at the order  $2n$ . When the two criteria (pertaining to natural frequency and damping ratios) are simultaneously met at the order  $2n$ , the identified modal parameters are considered “stable”, and a marker is drawn at the point in the stability diagram, whose horizontal and vertical positions correspond to  $2n$  and the identified natural frequency, respectively. In this work, the criteria for frequencies and damping ratios were set as 1% and 5%, respectively, and was set as 50. Figure 11 shows a typical stability diagram for the current study using the Y-direction results. Figure 11a shows the calculation order as a function of frequency, which shows three vibration modes. Figure 11b shows the damping ratio as a function of the vibration frequencies indicating less obvious vibration modes. This observation has important implications for the automation of the mode identification process, which is discussed below.

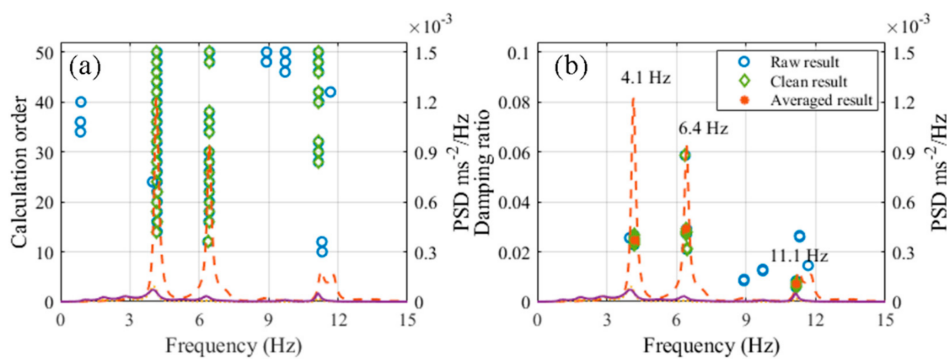


**Figure 11.** Stabilization diagram using the stochastic subspace identification (SSI) method and identified vibration parameters: (a) calculation order as a function of frequency; (b) damping ratio as a function of frequency (raw results—prior to pole-picking algorithm; clean results—after application of pole-picking algorithm).

### 3.3. Automatic Pole-Picking Procedure

Since long term monitoring produces a significant amount of data, to facilitate data analysis, the vibration parameters need to be identified using automated procedures. Automated modal analysis procedures based on the stochastic subspace identification (SSI) method were used [33–35]. Methods based on clustering adopt a stability diagram; therefore, they can be used concurrently with

commercial modal analysis software [33,35]. In this study, a new cluster method was adopted for the automated process. The cluster method does not require iteration and costs less calculation time.

With the SSI method, poles corresponding to different calculation orders can be obtained. Each pole contains the information on frequency, damping ratio, and mode shape. The similarity between different orders of calculated mode shapes is evaluated by a parameter called the modal assurance criterion (MAC). In this work, the number of poles clustered within a certain frequency and MAC range was called a local density  $\rho$ , and a value was assigned to the cluster. The pole-picking procedure uses the local density and its distance to the other poles to define the cluster. It can be presented as follows [36]:

- (1) Calculate frequency distances  $d_{ij}$  and  $MAC_{ij}$  between each pole set,  $i$  and  $j$ :

$$d_{ij} = \left| \frac{f_i - f_j}{f_j} \right|; \tag{15}$$

$$MAC_{ij} = \frac{(\boldsymbol{\varphi}_i^T \boldsymbol{\varphi}_j)^2}{(\boldsymbol{\varphi}_i^T \boldsymbol{\varphi}_i)(\boldsymbol{\varphi}_j^T \boldsymbol{\varphi}_j)} \tag{16}$$

- (2) If  $d_{ij}$  and  $MAC_{ij}$  satisfy the following criteria, then add one to the local density value  $\rho_i$  of pole  $i$ :

- $d_{ij} \times 100\% < 1\%$ ;
- $(1 - MAC_{ij}) \times 100\% < 1\%$ .

- (3) Pick the poles with relatively high local densities.

In this work, only poles with a local density  $\rho_i$  higher than five were used. Averages of clean poles corresponding to different modes were then identified as final results.

Figure 12 summarizes the pole-picking algorithm for mode identification. The values defined in the two selection processes should be determined based on a proper understanding of the behaviors of the particular structure and the serviceability (limits on vibration amplitudes) requirements. The selection of the criteria range will not critically impact the number of “stable” modes that can be identified.

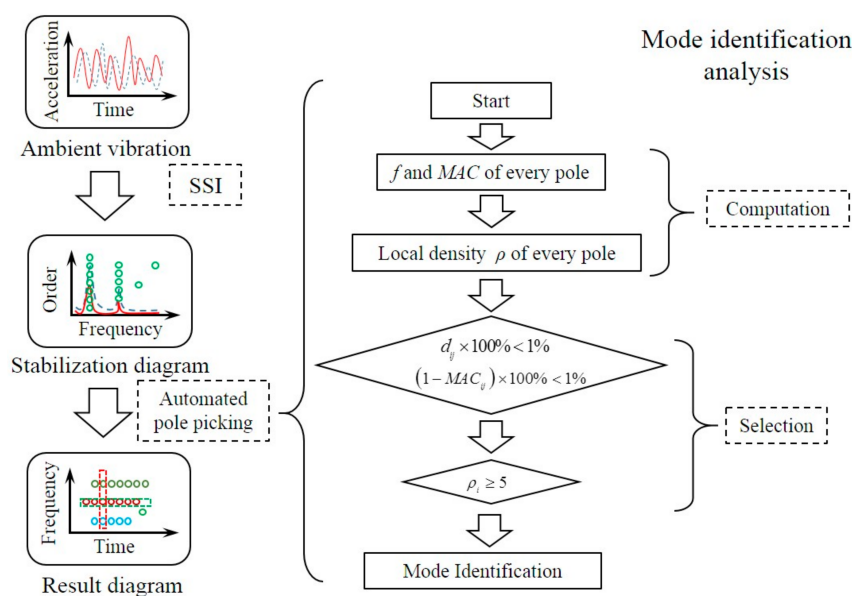
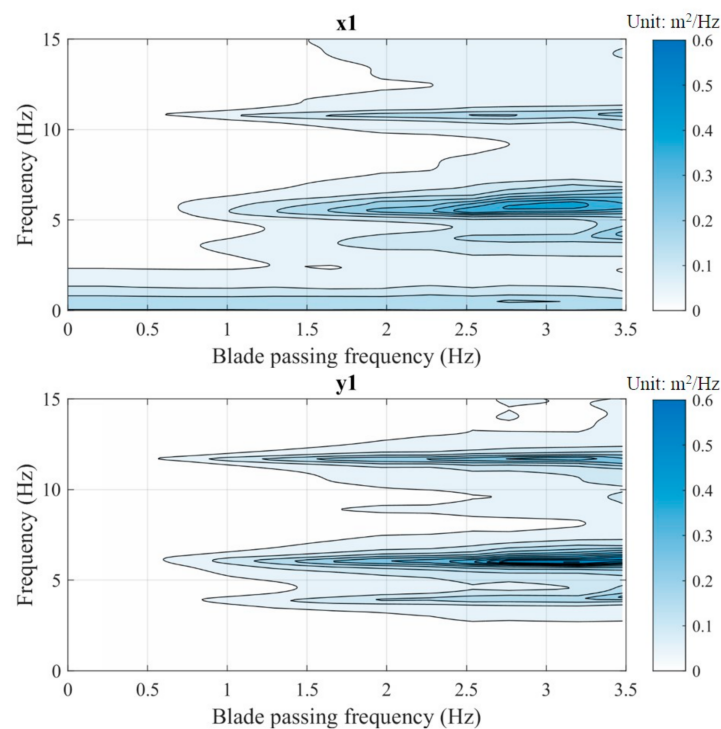


Figure 12. Flow chart of the proposed pole-picking approach.

## 4. Results and Discussion

### 4.1. Vibration Composition Analysis

The VAWT vibration is fundamentally caused by wind force, but the vibration amplitudes did not show a strong correlation with wind speed, since the measured excitations and responses were not of the same phase. To determine how the wind turbine vibration signature changed, the PSD diagrams of the turbine vibration accelerations along both the X- and Y-directions of cross Section 1 were presented along with the turbine rotation speed (transferred into blade passing frequencies to indicate whether there were excitations caused by blade rotation) in contour plots, and are shown in Figure 13. Measurements on 28 August 2016 were used for the analysis. It was first noted that there were little changes in the frequency values associated with the rotation speeds; thus, it was concluded that the rotation of blades did not cause significant disturbances on the global structural mode identification, which is unlike the HAWTs [16,18]. However, it was also noted that the PSD amplitude of this VAWT vibration increased with an increase in rotation speed.



**Figure 13.** Vibration amplitude versus turbine blade passing frequency.

PSDs from the acceleration time histories were obtained from the #6 building roof (Station 2, which was close to the VAWT) and the wind turbine tower. Figure 14 shows the vibration PSDs of the building and the tower superimposed. Measurements of cross Section 1 along both the X-direction and the Y-direction were taken as references since their vibration amplitudes were the biggest and led to higher signal-to-noise ratios. Because the sensors deployed on the tower were less sensitive toward low-frequency responses, the relationships of the dynamic responses between the building and the tower under 2 Hz was ignored. Three peaks at 3.6, 5.6, and 11.7 Hz can be observed in Figure 14 along the X-direction. For the Y-direction, peaks at 3.8, 6.0, and 11.7 Hz can be seen in Figure 14.

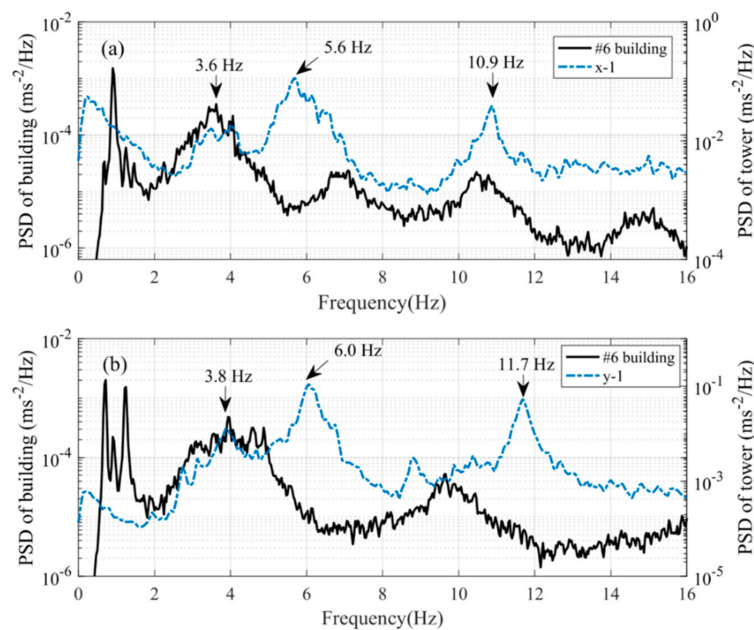


**Figure 14.** Comparison of acceleration PSDs measured from the roof of the #6 building and the VAWT: (a) X-direction; (b) Y-direction.

A closer observation of Figure 14 shows that some modes are closely associated with the building vibration frequencies; hence, they can be identified as building-associated modes. Specifically, the 3.6 and 3.8 Hz modes of the tower along both the X- and Y-directions have corresponding peaks that match the vibration mode of the #6 building (see also Table 2). On the other hand, the peaks at 5.8 Hz and 6.0 Hz along the X- and Y-directions, respectively, are the fundamental frequencies of the wind turbine tower, and they are unique as the corresponding PSD values of the #6 building do not exist. This indicates that the building contributed to the vibration of the tower.

Table 6 summarizes the vibration frequencies identified along both the X- and Y-directions. Due to the rotation of the deflector and the H-shape blades, frequencies of some modes can fluctuate within a narrow range.

**Table 6.** Vibration frequencies of the tower.

Direction	Frequency (Hz)			
	1st	2nd	3rd	4th
x	3.6	5.8	10.7	
y	3.8	6.0	9.7	11.7

According to Figures 13 and 14, 5.6 Hz and 6.0 Hz were the domain frequencies of the VAWT vibration along the X-direction and Y-direction, respectively. The predominant building-associated VAWT vibration modes were 3.6 Hz along the X-direction and 3.8 Hz along the Y-direction since peaks with the same frequencies can be found in the PSD curves of the building vibrations. The third mode frequency of the building along the X-direction was 6.9 Hz, and it influenced the VAWT vibration, since the contour plot was sparser above 5.6 Hz than below 5.6 Hz, as shown in in Figure 13 (x1 plot).

Although the influence cannot be seen clearly in Figure 14, a 9.6-Hz mode, which is the fourth peak along the Y-direction building PSD curve, shows an obvious contour in Figure 14 (y1 plot). Furthermore, a 10.9 Hz mode along the X-direction and 11.7 Hz along the Y-direction are actual VAWT vibration modes. This 10.9-Hz (along the X-direction) VAWT vibration is very close to the fourth building vibration mode along the X-direction with a frequency of 10.6 Hz.

#### 4.2. Mode Identification

Data from 26 August to 4 September 2016 were used to generate the scatter plots for mode identification with the automated algorithm introduced in Section 3, which are shown in Figure 15. Because most of the modes are shown as scattered data points, a line fit was used to help determine the specific frequencies (colored scatters) of interest. It can be found that, generally, the concerned frequencies decreased as the temperature or blade passing speed increased. Usually, the high temperature and severe vibration of the structure may reduce the rigidity of the system due to steel material characteristics and the boundary feature of the VAWT. Wind direction has little influence on the vibration frequencies as the VAWT is insensitive to the incoming flow. The influence of the blade passing speed on the vibration frequency is not as strong as that of the wind speed. The reason can be that the change of rotation speed lags behind the airflow velocity change.

The identified mode shapes along both the X-direction (hoop bolt shear) and the Y-direction (hoop bolt tension) of the tower are shown in Figure 16. Superimposed in the amplitude plots (Figure 16) are the idealized mode shapes. According to Reference [8], the mode shapes of the  $\Phi$ -type VAWT shaft are combinations of a simply supported beam and a cantilever. However, this  $\Phi$ -type VAWT was attached with cables, which is different from the H-type VAWT we studied. A laboratory experimental study was conducted with an H-type VAWT in Reference [9]. However, it does provide mode shapes of the VAWT. A stereo vision technique was used to measure a  $\Phi$ -type VAWT vibration in Reference [11], and the mode shapes of the  $\Phi$ -type VAWT shaft were also cantilevers. However, the mode shapes of the H-type VAWT shaft in our study are not completely cantilever shapes since the shaft was connected with two bearings, which cannot be simplified as totally rigid boundary conditions.

It is important to point out that the mode shape corresponding to 9.7 Hz along the Y-direction was different from the others, with the vibration amplitude of the topmost section (cross Section 1) smaller than that of the bottom section (cross Section 3). This mode is a building-associated mode, but the vibration of the shaft is at an opposite phase with the building; thus, the vibration on the top is counteracted. Also shown in Figure 16 are the views from the top of the vibration modes.

The differentiation between building-associated and non-building-associated modes implies that, for future condition monitoring, these two types of modes can be separately studied to identify the influence of building vibration to the tower vibration and to study the tower-alone vibration. The building-associated modes may indicate the PSD or amplitude effects on the VAWT vibration, and the non-building-associated modes would indicate the connections and overall integrity of the VAWT.

Finally, the fundamental frequency along the Y-direction (tension direction of the hoop bolts) was consistent with the calculated values, which was 6.0 Hz. However, the frequency corresponding to the X-direction (shear direction of the hoop bolts) was lower than the calculated value, which was 7.2 Hz. This may be because of an overestimation of the connection stiffness in the theoretical model.

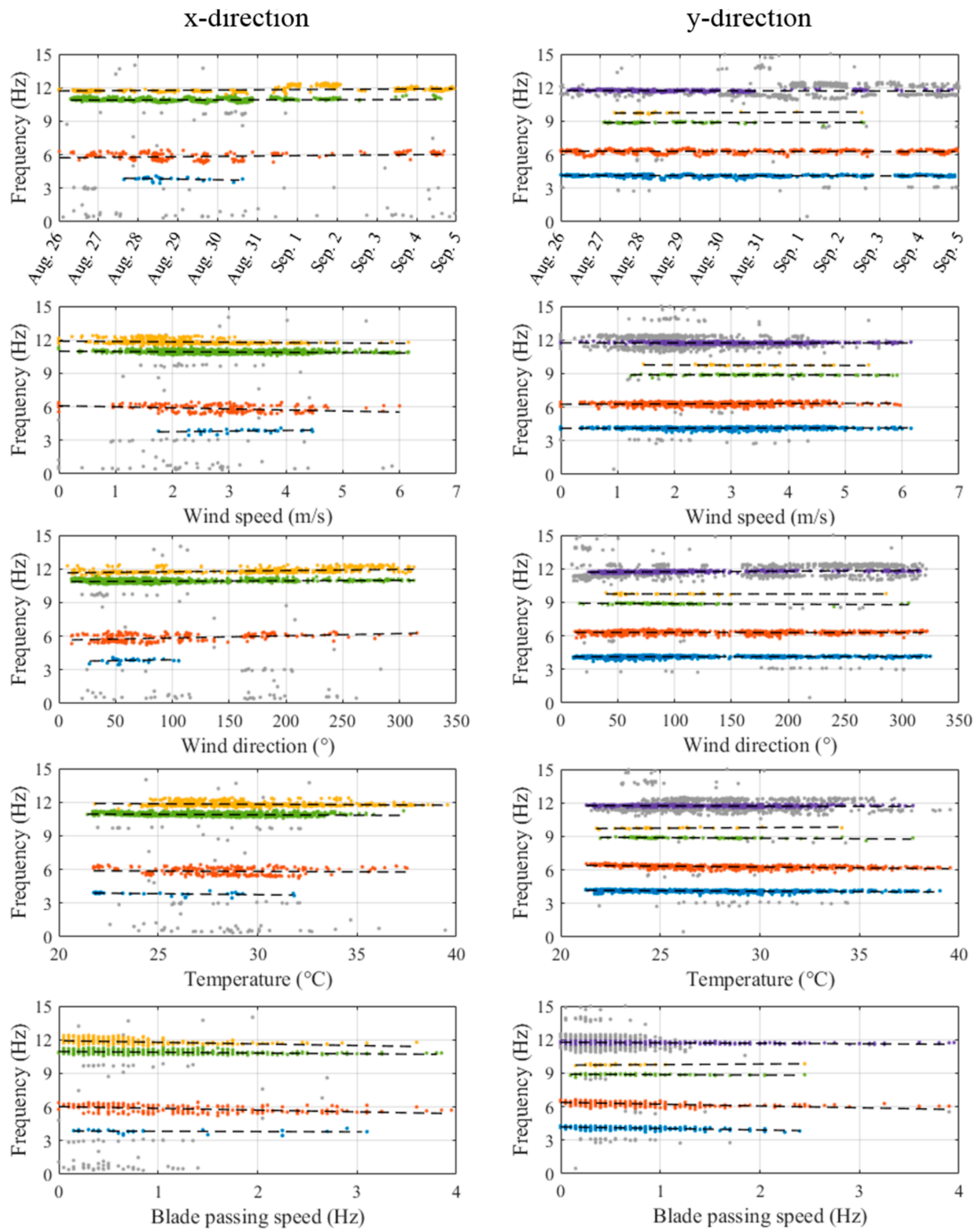
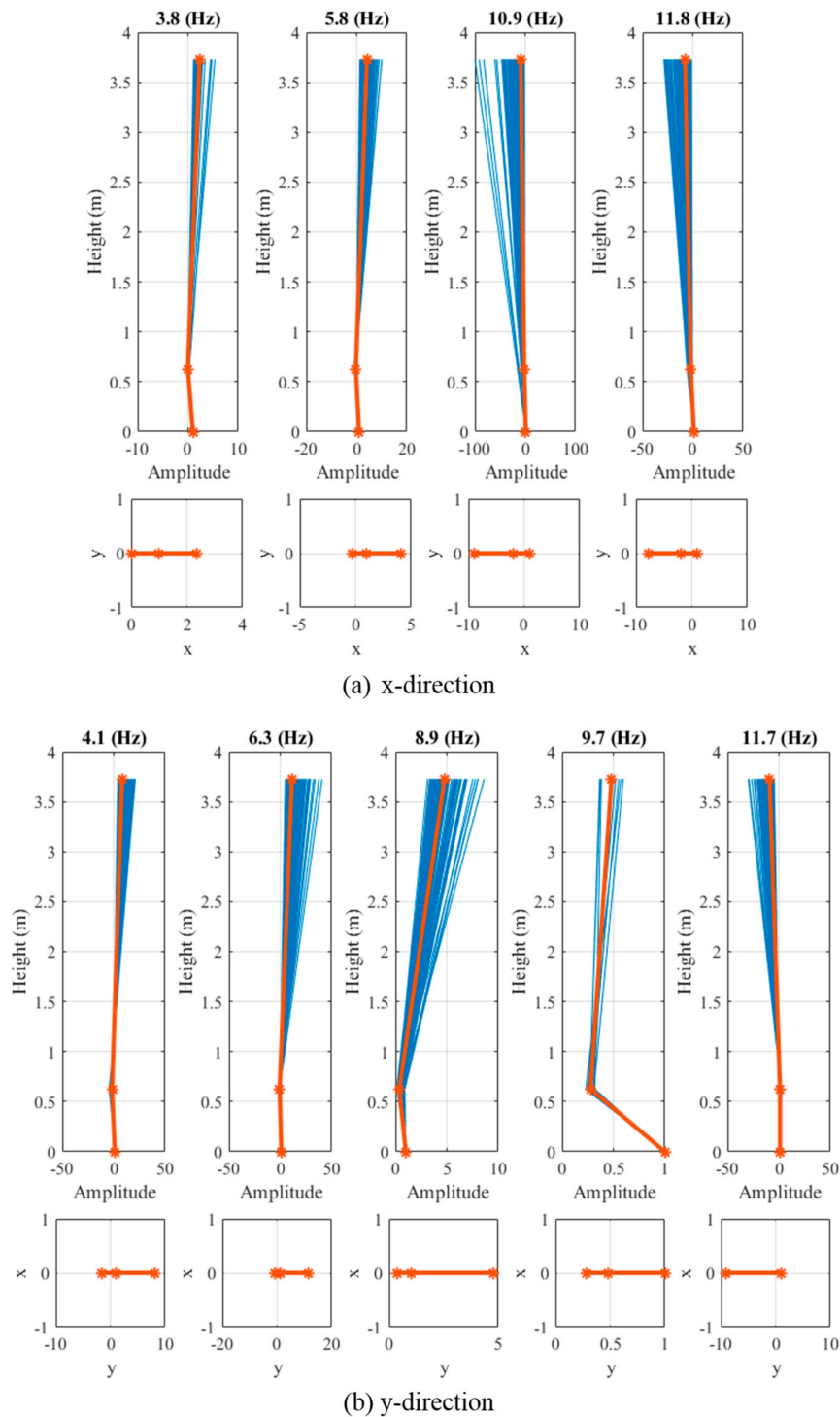


Figure 15. Ambient parameter effects on tower vibrations (26 August to 4 September).



**Figure 16.** Identified mode shapes and the associated schematics of the four dominant modes along (a) the X-direction, and (b) the Y-direction (26 August to 4 September).

### 5. Conclusions

This paper presents a field vibration study of an H-type VAWT on a rooftop. To understand the vibration performances of the VAWT installed on the rooftop of the #6 building at Tongji University, a health monitoring system was implemented, and the dynamic behaviors of the VAWT were studied using vibration measurements under ambient conditions. To process the vibration data, an automated algorithm based on stochastic subspace identification (SSI) and a fast clustering approach was

developed and presented to show how modes could be determined. The modified method helps accommodate the frequency and mode shape requirements for mode identification, and the results successfully identified several modes of the VAWT tower vibration along the tension direction and shear direction of the hoop connection.

The results showed that some of the vibration responses of the VAWT tower (e.g., 3.6 Hz along the X-direction and 3.8 Hz along the Y-direction) may be affected by the vibrations of the #6 building. Hence, the modal behaviors can be differentiated into building-associated and non-building-associated modes. Among the vibration frequencies identified from both the building and tower measurements, the first mode vibration of the building (0.94 Hz along the X-direction, 0.71 Hz along the Y-direction, and 1.3 Hz in torsion) has little influence on tower vibration. The second bending modes of the building along both directions (3.6 Hz along the X-direction and 4.1 along the Y-direction), however, can affect tower vibration, since the frequencies of the second mode of the building are relatively close to those fundamental frequencies of the tower. This observation is important for the structural health monitoring and life-cycle condition maintenance strategy of the VAWT. The understanding of the effect of building-associated and non-building-associated modes on the VAWT tower responses may also help improve the design of the VAWT tower.

The environmental effects on the ambient vibration data were also investigated, and it was found that the blade rotation speed had a significant effect on the VAWT vibration PSD amplitudes, as shown in Figure 13, indicating that higher blade rotation speeds can result in higher vibration amplitudes of the wind turbine. On the other hand, temperature and wind direction, in general, had little effect on the PSD amplitudes.

**Author Contributions:** Y.W. analyzed the monitoring data and prepared the manuscript. W.L. is the principal investigator of this project. K.D. is the leading author of this manuscript and prepared the original draft together with the first author. M.Y. helped collect data and S.-E.C. helped with paper writing, reviewing & editing.

**Acknowledgments:** This research was funded by the International Collaboration Program of Science and Technology Commission of Ministry of Science and Technology, China (Grant No. 2016YFE0105600), the International Collaboration Program of Science and Technology Commission of Shanghai Municipality and Sichuan Province (Grant Nos. 16510711300 and 18GJHZ0111), the National Natural Science Foundation of China (Grant No. U1710111), the Fundamental Research Funds for Central Universities of China, and the China Scholarship Council.

**Conflicts of Interest:** The authors declare no conflicts of interest.

## Abbreviations

HAWT	horizontal axis wind turbine;
VAWT	vertical axis wind turbine;
SHM	structural health monitoring;
SSI	stochastic subspace identification;
PSD	power spectrum density;
MAC	modal assurance criterion.

## Symbols

$k_t$	tensile stiffness of a single hoop;
$k_s$	shear stiffness of a single hoop;
$k_{M10}, k_{M12}$	tensile stiffness of M10 bolt and M12 bolt, respectively;
$k_R$	compression stiffness of the rubber gasket;
$k_{M12,s}$	shear stiffness of the M12 bolt;
$\mathbf{P}_{XX}(f)$	PSD of the response of a structure;
$\mathbf{T}(f)$	transfer function;
$\mathbf{I}$	unit matrix;
$x_k$	state vector;
$y_k$	measurement vector;
$w_k$	excitation vector;

$v_k$	measurement noise vector;
$\mathbf{A}$	state transition matrix;
$\mathbf{C}$	output location matrix;
$k_t$	number of measurement;
$\mathbf{H}$	Hankel matrix;
$\mathbf{O}$	projection matrix;
$\mathbf{\Gamma}$	observability matrix;
$\hat{\mathbf{X}}$	Kalman filter state sequence;
$\lambda$	eigenvalue of $\mathbf{A}$ ;
$\Psi$	eigenvector of $\mathbf{A}$ ;
$f_s$	sampling frequency;
$2n$	maximum calculation order;
$f$	natural frequency;
$\zeta$	damping ratio;
$\varphi$	mode shape;
$\rho$	local density of a result point;
$d$	frequency distance between two result points;
MAC	mode shape similarity (modal assurance criterion) between two result points.

## References

- Riegler, H. HAWT versus VAWT: Small VAWTs find a clear niche. *Refocus* **2003**, *4*, 44–46.
- Han, D.; Heo, Y.G.; Choi, N.J.; Nam, S.H.; Choi, K.H.; Kim, K.C. Design, Fabrication, and Performance Test of a 100-W Helical-Blade Vertical-Axis Wind Turbine at Low Tip-Speed Ratio. *Energies* **2018**, *11*, 1517. [[CrossRef](#)]
- Marie, D.G.J. Turbine Having its Rotating Shaft Transverse to the Flow of the Current. U.S. Patent No. 1,835,018, 8 December 1931.
- Bhutta, M.M.A.; Hayat, N.; Farooq, A.U.; Ali, Z.; Jamil, S.R.; Hussain, Z. Vertical axis wind turbine—A review of various configurations and design techniques. *Renew. Sustain. Energy Rev.* **2012**, *16*, 1926–1939. [[CrossRef](#)]
- Jin, X.; Zhao, G.; Gao, K.J.; Ju, W. Darrieus vertical axis wind turbine: Basic research methods. *Renew. Sustain. Energy Rev.* **2015**, *42*, 212–225. [[CrossRef](#)]
- Yang, Y.; Guo, Z.; Zhang, Y.; Jinyama, H.; Li, Q. Numerical Investigation of the Tip Vortex of a Straight-Bladed Vertical Axis Wind Turbine with Double-Blades. *Energies* **2017**, *10*, 1721. [[CrossRef](#)]
- Mabrouk, I.B.; Hami, A.E.; Walha, L.; Zghal, B.; Haddar, M. Dynamic vibrations in wind energy systems: Application to vertical axis wind turbine. *Mech. Syst. Signal Process.* **2017**, *85*, 396–414. [[CrossRef](#)]
- James, G.H.I.; Carne, T.G.; Lauffer, J.P. *The Natural Excitation Technique (NExT) for Modal Parameter Extraction from Operating Wind Turbines*; Nasa STI/Recon Technical Report N; 1993; Volume 93, pp. 260–277. Available online: <https://prod.sandia.gov/techlib-noauth/access-control.cgi/1992/921666.pdf> (accessed on 7 June 2018).
- Mclaren, K.; Tullis, S.; Ziada, S. Measurement of high solidity vertical axis wind turbine aerodynamic loads under high vibration response conditions. *J. Fluids Struct.* **2012**, *32*, 12–26. [[CrossRef](#)]
- Malge, A.; Pawar, P. Wind tunnel and numerical performance analysis of multi-storey vertical axis wind turbines. *J. Renew. Sustain. Energy* **2015**, *7*, 053121. [[CrossRef](#)]
- Najafi, N.; Paulsen, U.S. Operational modal analysis on a VAWT in a large wind tunnel using stereo vision technique. *Energy* **2017**, *125*, 405–416. [[CrossRef](#)]
- Rankine, R.K.; Chick, J.P.; Harrison, G.P. Energy and carbon audit of a rooftop wind turbine. *Proc. Inst. Mech. Eng. A J. Power Energy* **2006**, *220*, 643–654. [[CrossRef](#)]
- Balduzzi, F.; Bianchini, A.; Carnevale, E.A.; Ferrari, L.; Magnani, S. Feasibility analysis of a Darrieus vertical-axis wind turbine installation in the rooftop of a building. *Appl. Energy* **2012**, *97*, 921–929. [[CrossRef](#)]
- Brownjohn, J.M. Structural health monitoring of civil infrastructure. *Philos. Trans. R. Soc. Lond. A Math. Phys. Eng. Sci.* **2007**, *365*, 589–622. [[CrossRef](#)] [[PubMed](#)]

15. Ou, J.; Li, H. Structural health monitoring in mainland china: Review and future trends. *Struct. Health Monit.* **2010**, *9*, 219–231.
16. Lan, C.; Li, H.; Ou, J. Traffic load modelling based on structural health monitoring data. *Struct. Infrastruct. Eng.* **2011**, *7*, 379–386. [[CrossRef](#)]
17. Rohrmann, R.G.; Thöns, S.; Rücker, W. Integrated monitoring of offshore wind turbines—Requirements, concepts and experiences. *Struct. Infrastruct. Eng.* **2010**, *6*, 575–591. [[CrossRef](#)]
18. Smarsly, K.; Hartmann, D.; Law, K.H. A computational framework for life-cycle management of wind turbines incorporating structural health monitoring. *Struct. Health Monit.* **2013**, *12*, 359–376. [[CrossRef](#)]
19. Shirzadeh, R.; Devriendt, C.; Bidakhvidi, M.A.; Guillaume, P. Experimental and computational damping estimation of an offshore wind turbine on a monopile foundation. *J. Wind Eng. Ind. Aerodyn.* **2013**, *120*, 96–106. [[CrossRef](#)]
20. Devriendt, C.; Weijtjens, W.; El-Kafafy, M.; De Sitter, G. Monitoring resonant frequencies and damping values of an offshore wind turbine in parked conditions. *IET Renew. Power Gener.* **2014**, *8*, 433–441. [[CrossRef](#)]
21. Hu, W.H.; Thöns, S.; Rohrmann, R.G.; Said, S.; Rücker, W. Vibration-based structural health monitoring of a wind turbine system. Part I: Resonance phenomenon. *Eng. Struct.* **2015**, *89*, 260–272. [[CrossRef](#)]
22. Hu, W.H.; Thöns, S.; Rohrmann, R.G.; Said, S.; Rücker, W. Vibration-based structural health monitoring of a wind turbine system Part II: Environmental/operational effects on dynamic properties. *Eng. Struct.* **2015**, *89*, 273–290. [[CrossRef](#)]
23. Dai, K.; Wang, Y.; Huang, Y.; Zhu, W.; Xu, Y. Development of a modified stochastic subspace identification method for rapid structural assessment of in-service utility-scale wind turbine towers. *Wind Energy* **2017**, *20*, 1687–1710. [[CrossRef](#)]
24. Weijtjens, W.; Verbelen, T.; Sitter, G.D.; Devriendt, C. Foundation structural health monitoring of an offshore wind turbine—A full-scale case study. *Struct. Health Monit.* **2016**, *15*, 389–402. [[CrossRef](#)]
25. Loh, C.H.; Loh, K.J.; Yang, Y.S.; Hsiung, W.Y.; Huang, Y.T. Vibration based system identification of wind turbine system. *Struct. Control Health Monit.* **2017**, *24*, e1876. [[CrossRef](#)]
26. Dai, K.; Huang, Y.; Gong, C.; Huang, Z.; Ren, X. Rapid seismic analysis methodology for in-service wind turbine towers. *Earthq. Eng. Eng. Vib.* **2015**, *14*, 539–548. [[CrossRef](#)]
27. Dai, K.; Sheng, C.; Zhao, Z.; Yi, Z.; Camara, A.; Bitsuamlak, G. Nonlinear response history analysis and collapse mode study of a wind turbine tower subjected to cyclonic winds. *Wind Struct.* **2017**, *25*, 79–100.
28. Qu, L. Analysis on Structural Interaction between Highrise Building and Roof-Mounted Wind Turbine Generator. Master's Thesis, Tongji University, Shanghai, China, 2015. (In Chinese)
29. Bingham, C.; Godfrey, M.; Tukey, J.W. Modern techniques of power spectrum estimation. *IEEE Trans. Audio Electroacoust.* **1967**, *15*, 56–66. [[CrossRef](#)]
30. Bendat, J.S.; Piersol, A.G. *Random Data: Analysis and Measurement Procedures*; Wiley and Sons, Inc.: Hoboken, NJ, USA, 1971.
31. Van Overschee, P.; De Moor, B. Subspace algorithms for the stochastic identification problem. *Automatica* **1993**, *29*, 649–660. [[CrossRef](#)]
32. Peeters, B.; Roeck, G.D. Reference-based stochastic subspace identification for output-only modal analysis. *Mech. Syst. Signal Process.* **1999**, *13*, 855–878. [[CrossRef](#)]
33. El-Kafafy, M.; Devriendt, C.; Guillaume, P.; Helsen, J. Automatic tracking of the Modal parameters of an offshore wind turbine drivetrain system. *Energies* **2017**, *10*, 574. [[CrossRef](#)]
34. Zhang, Y.; Kurata, M.; Lynch, J.P. Long-term modal analysis of wireless structural monitoring data from a suspension bridge under varying environmental and operational conditions: System design and automated modal analysis. *J. Eng. Mech. ASCE* **2016**, *143*, 04016124. [[CrossRef](#)]
35. Cabboi, A.; Magalhães, F.; Gentile, C.; Álvaro, C. Automated modal identification and tracking: Application to an iron arch bridge. *Struct. Control Health Monit.* **2017**, *24*, e1854. [[CrossRef](#)]
36. Rodriguez, A.; Laio, A. Clustering by fast search and find of density peaks. *Science* **2014**, *344*, 1492–1496. [[CrossRef](#)] [[PubMed](#)]

